journal of the mechanical behavior of biomedical materials 139 (2023) 105660

Contents lists available at ScienceDirect

Journal of the Mechanical Behavior of Biomedical Materials

journal homepage: www.elsevier.com/locate/jmbbm

Investigating the post-yield behavior of mineralized bone fibril arrays using a 3D non-linear finite element unit-cell model

Elham Alizadeh [a,*], Sadik Omairey [b], Philippe Zysset [a]

[a] ARTORG Centre for Biomedical Engineering Research, University of Bern, Bern, Switzerland
[b] Brunel Composites Centre, College of Engineering, Design and Physical Sciences, Brunel University London, London, UK

ARTICLE INFO

Keywords:
Fibril array
Cohesive interaction
Finite element model
Bone
Post-yield behavior
Plasticity
Experimental validation
Extrafibrillar matrix
Mineralized collagen fibril

ABSTRACT

In this study, we propose a 3D non-linear finite element (FE) unit-cell model to investigate the post-yield behavior of mineralized collagen fibril arrays (FAY). We then compare the predictions of the model with recent micro-tensile and micropillar compression tests in both axial and transverse directions. The unit cell consists of mineralized collagen fibrils (MCFs) embedded in an extrafibrillar matrix (EFM), and the FE mesh is equipped with cohesive interactions and a custom plasticity model. The simulation results confirm that MCF plays a dominant role in load bearing prior to yielding under axial tensile loading. Damage was initiated via debonding in shear and progressive sliding at the MCF/EFM interface, and resulted in MCF pull-out until brittle failure. In transverse tensile loading, EFM carried most of the load in pre-yield deformation, and then mixed normal/shear debonding between MCF and EFM began to form, which eventually produced brittle delamination of the two phases. The loading/unloading FE analysis in compression along both axial and transverse directions demonstrated perfect plasticity without any reduction in elastic modulus, i.e., damage due to the interfaces as seen in micropillar compression. Beyond the brittle and ductile nature of the stress–strain curves, in tensile and compressive loading, the simulated post-yield behavior and failure mechanism are in good quantitative agreement with the experimental observations. Our rather simple but efficient unit-cell FE model can reproduce qualitatively and quantitatively the mechanical behavior of bone ECM under tensile and compressive loading along the two main orientations. The model's integration into higher length scales may be useful in describing the macroscopic post-yield and failure behavior of trabecular and cortical bone in greater detail.

1. Introduction

Bone stiffness plays a main role in musculoskeletal function while its strength and the ability to dissipate energy protect vital organs such as the brain, lungs, and heart (Weiner et al., 1999; Fratzl and Weinkamer, 2007). Bone is a hierarchically structured bio-composite (Fig. 1) with various toughening mechanisms from the nanoscale to the macroscale (Rho et al., 1998; Reznikov et al., 2014). Type I collagen and hydroxyapatite platelets (HA), which are regarded as the basic constituents of bone, form mineralized collagen fibrils (MCF) embedded in an extrafibrillar matrix (EFM). The EFM, which is made of mineral particles coated with non-collagenous proteins (NCP) (Currey, 2013), and MCF are arranged into parallel fibril arrays (FAY) at the sub-microscale (Olszta et al., 2007; Hang and Barber, 2011). At the microscale, the lamellar structural units such as osteons and circumferential lamellae in compact bone or packets in trabecular bone are formed by different arrangements of FAY (Aoubiza et al., 1996; Dong and Guo, 2006; Parnell and Grimal, 2009). The mesoscale refers to cortical bone and porous trabecular bone, while the macroscale refers to the entire bone level (Nikel et al., 2018).

Bone diseases such as osteoporosis have major physical, psychosocial, and economic consequences, leading to a major socio-economic challenge in aging populations. A comprehensive understanding of the structure-mechanical properties and failure mechanism relationships of bone at different hierarchical scales may help to improve prevention, diagnosis and treatment of these diseases. The sub-micro-scale, which hosts the same FAY unit in cortical and trabecular bone, is one of the interesting length scales for explaining the underlying mechanisms of bone fracture. Thus, studying FAY post-yield behavior and quantifying how morphological variations at the sub-micro scale due to disease, aging, and treatment affect fracture processes at larger length scales could be beneficial (Hamed and Jasiuk, 2013).

* Corresponding author.
E-mail address: elham.alizadeh@unibe.ch (E. Alizadeh).

https://doi.org/10.1016/j.jmbbm.2023.105660
Received 2 November 2022; Received in revised form 24 December 2022; Accepted 4 January 2023
Available online 6 January 2023

A few studies investigated the elastic modulus of bone ECM using basic models such as Voigt, Reuss or shear lag (Jäger and Fratzl, 2000), continuum micromechanics theories (Fritsch and Hellmich, 2007; Nikolov and Raabe, 2008; Yoon and Cowin, 2008; Hamed et al., 2010; Reisinger et al., 2010) like the Mori and Tanaka scheme (MT) (Mori and Tanaka, 1973) or the self-consistent (SC) method (Hill, 1963; Budiansky, 1965), and finite element (FE) models (Jasiuk and Ostoja-Starzewski, 2004; Barkaoui et al., 2014).

Alizadeh et al. (Alizadeh et al., 2020) presented recently a two-scale 3D FE model of bone FAY in which a unit cell with periodic boundary conditions (BPC) was used to compute the apparent elastic properties under six canonical load cases. The FE models of bone ECM were calibrated using experimental tests on ovine micro-samples in both the axial and transverse directions (Schwiedrzik et al., 2014; Casari et al., 2021), and the FE results were compared to previous analytical methods. Beyond elastic properties, the FE models provide stress distribution within the MCF, EFM, and the resulting FAY and confirm the shear lag mechanisms at both hierarchical levels. A thorough sensitivity analysis reveals that the mineral volume fraction in the fibril array is the most influential parameter on the axial and transverse elastic moduli, and the MCF volume fraction in FAY is the most sensitive variable for the axial versus transverse elastic moduli ratio.

There are some FE models that evaluate the post-yield mechanical behavior of single MCFs as in (Buehler, 2007; Siegmund et al., 2008; Barkaoui and Hambli, 2011; Barkaoui et al., 2011; Luo et al., 2011; Hambli and Barkaoui, 2012; Nair et al., 2013). However, the number of FE studies on the mechanical behavior of FAY or MCF arrays is limited.

Hamed and Jasiuk presented a 2D FE model of bone ECM consisting of mineralized collagen fibril and water and evaluated the stress-strain response of FAY under tensile loading. The cohesive layer was placed at the interfaces of these two constituents to simulate damage within the FAY due to MCF sliding. The interaction was a weak one due to thick layer of water, and they assumed Van der Waals and viscous shear interactions, respectively, for normal and shear mode properties of the cohesive zone (Hamed and Jasiuk, 2013). Lai and Yann numerically investigated the mechanical behavior of FAY using a 2D finite element model (FEM) of MCF embedded in an extrafibrillar protein matrix and utilized a cohesive zone model to simulate the extrafibrillar protein matrix. Three-point bending tests were performed on the FAY model, and the effects of MCF dimensions and failure energy in EFM were evaluated by varying MCF lengths, aspect ratios, and thicknesses, as well as different cohesive laws in EFM (Lai and Yan, 2017). De Falco et al. developed a 2D finite element model of antler bone containing MCFs connected through cohesive interfaces. The FE results of mineralized fibrils subjected to cyclic loading were compared to the experimental results, and the staggered fibril arrangement and damageable interface were identified as key parameters in controlling antler bone hysteresis under cyclic loading (De Falco et al., 2017).

Wang and Ural evaluated the effect of MCF size and orientation on a 3D finite element model of bone ECM containing mineralized collagen fibrils and a layer of cohesive elements on the outer surfaces of the MCFs, which represent the extrafibrillar matrix as an interface between the fibrils (Wang and Ural, 2018b). They also investigated the influence of mineral content, mineral distribution, and interaction between MCFs under axial and transverse tensile loading using an FE model of an MCF network (Wang and Ural, 2019). Wang and Ural used the previously presented FE model of the MCF network in another study to assess the effect of changes in the mechanical properties of MCFs and EFMs on the mechanical behavior of bone FAY under tensile loading in the axial and transverse directions (Wang and Ural, 2018a).

Maghsoudi-Ganjeh et al. evaluated the mechanical behavior and failure mechanism of bone at the sub-lamellar level under compressive and tensile loading. They presented a 2D model in which the HA platelet was added to the collagen matrix with a layer of water and the mineral crystals bonded to each other with a thin layer of NCPs, forming the MCF and EFM, respectively (Maghsoudi-Ganjeh et al., 2019). The failure mechanism in compression began with relative sliding between HA crystals, and delamination between MCF and EFM and local buckling of MCF occurred as a result of shear bands. In tension, an array of mode-I nano-cracks appeared in model and as the applied load increased, the crack propagated leading to overall failure of model.

Xu and An proposed a 2D numerical model of FAY including the mineralized collagen fibrils embedded in an extrafibrillar matrix. Plastic deformation of MCF, plastic deformation of EFM, and a cohesive zone model of the interface between MCF and EFM were considered in the model. The effect of MCF and EFM material properties, plastic deformation in constituents, and interfaces between MCF and EFM on the energy dissipation of fibril arrays was investigated (Xu and An, 2020; An and Li, 2021).

The mechanical behavior of FAY was recently studied in a few unique experimental studies. Schwiedrzik et al. (2014) investigated the mechanical behavior of a single osteonal lamellae in ovine bone using micropillar compression tests in a scanning electron microscope (SEM). The ovine osteons showed the uniaxial fibril orientation by BF-STEM images.

(Schwiedrzik et al., 2017). The elastic modulus, yield stress, and failure mechanism of bone ECM were evaluated under monotonic and cyclic compression tests in both axial and transverse directions. Using micropillar compression tests, Ma et al. (2021) evaluated the mechanical behavior of bovine bone samples fabricated from three adjacent

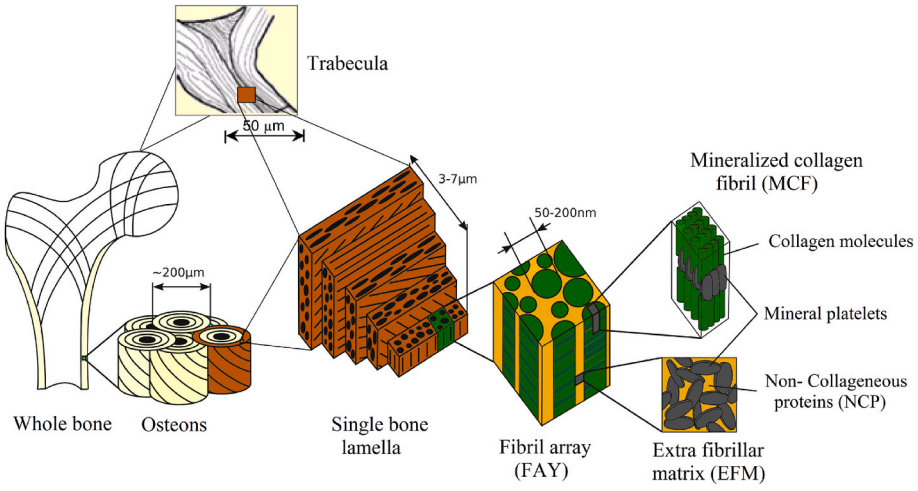

Fig. 1. Hierarchical structure of bone.

layers of single osteons. Using the proposed deformation theory, the effect of collagen fibril orientation on the mechanical behavior of the micropillar was investigated.

Recently, Casari et al. (2019) presented a novel technology for investigating the mechanical behavior of specimens at the micro-scale under uniaxial tensile loading. The sample geometry was optimized using FE analysis, and the micro-tensile set-up promoted self-alignment to prevent stress concentrations outside the specimen gauge. Then, the setup was used to evaluate the mechanical behavior of ovine bone at the FAY level under tensile loading in both axial and transverse directions (Casari et al., 2021).

The experimental results on ovine bone obtained by micro-tensile (Casari et al., 2021) and micropillar compression tests (Schwiedrzik et al., 2014) at the same scale and for the same tissue revealed the first experimental results of bone's mechanical behavior at the FAY level under tension-compression loading in the axial and transverse directions.

Another experimental study conducted by Fantler et al. revealed the separation between MCFs connected through extrafibrillar matrix at the FAY level (Fantner et al., 2005). Indeed, the bonds between MCFs break and the mineralized collagen fibrils separate from each other (Hassenkam et al., 2004; Thurner et al., 2007). Hang et al. used in situ atomic force microscopy to perform a fibril pull-out test on antler bone, which confirmed the antler bone's weak MCF-EFM interfaces (Hang et al., 2014).

Most of the finite element models presented in the literature were 2D simulations based on a large number of unverifiable assumptions, particularly in the form of cohesive element parameters, and were not properly validated with experimental results under both compression and tension, as well as along the FAY's axial and transverse directions.

Accordingly, this work aims to extend the 3D unit-cell model of FAY proposed by Alizadeh et al. (Alizadeh et al., 2020), which was previously calibrated with experiments in the elastic regime (Schwiedrzik et al., 2014; Casari et al., 2021), to investigate for the first time the post-yield behavior and damage mechanisms of bone ECM along axial and transverse directions in both tensile and compressive loading. Plasticity and cohesive interfaces are used to study residual strain and damage accumulation, respectively. Furthermore, a quantitative comparison with recent experiments is sought for all available loading cases.

2. Materials and methods

The periodic unit-cell FE model of the FAY, the elastic and plastic properties of the constituents, and the properties of the cohesive interfaces between MCF and EFM are described in this section.

2.1. Finite element analysis

A three-dimensional finite element model was designed using the commercial FE program ABAQUS (Hibbitt, 2013; Dassault Systems, 2014) to simulate the mechanical behavior and the failure mechanism of bone ECM. The solid continuum element—C3D8—a linear hexahedral eight-node brick element—comprising eight nodes with three translational degrees of freedom at each node with a maximum element size of 10 nm, was used in the FAY model. The element size was selected based on the mesh convergence study in which the ultimate strength changed with an error of 0.05% by dividing the original element size (10 nm) by 1.5. The overall damage mechanism and plastic behavior of the FAY did not change in convergence study.

The element is applicable for different nonlinear analyses, like those of large deformation, contact, plasticity, and failure. It is also appropriate for avoiding shear locking problem. The geometrical nonlinearity of the analysis was enabled in the software by selecting the "Nlgeom" option.

2.2. Fibril array model

In our previous research (Alizadeh et al., 2020), a two-scale unit-cell model of bone at sub-micro level consisting of mineralized collagen fibril (MCF) and extrafibrillar matrix (EFM) resulting in fibril array (FAY) was developed and calibrated with experimental results (Schwiedrzik et al., 2014; Casari et al., 2021) at the same scale to represent the elastic properties of bone ECM (Fig. 2).

A unit cell with a width and height of 105.4 nm and 182 nm, respectively, was designed where the MCFs were arranged with hexagonal symmetry. The ratio of height to width of the hexahedral unit cell was assumed $\sqrt{3}$ for compatibility with a hexagonal pattern. The central MCF and the four quarters of MCF in the corners had a radius of 50 nm, an aspect ratio of 100 nm, and were surrounded by EFM to form the FAY model. Gap zones of 200 nm were assumed in the middle part of the central MCF and at both ends of the corner MCFs that were filled with EFM. A volume fraction of 0.8 was considered for MCF in the FAY. The density of HA was considered approximately 3.1 $\frac{g}{cm^3}$ and the density of collagen and NCP were assumed almost 1.18 $\frac{g}{cm^3}$, thus the volume fraction of HA in FAY was selected as 0.423 to maintain the tissue density around 2 $\frac{g}{cm^3}$.

To simulate the observed brittle and ductile behavior in bone ECM micro samples under tensile and compressive loading, respectively, cohesive interactions were placed in model and plasticity model was assumed for both MCF and EFM phases. The following sections describe the mechanical properties of the phases, specifically the plasticity model and the cohesive interfaces.

2.3. Material properties

Table 1 shows the elastic properties of the transverse isotropic MCF and isotropic EFM phases used in the FE analyses.

A user material code (UMAT) (Schwiedrzik and Zysset, 2013) was exploited to model the plasticity of MCF and EFM in which an eccentric elliptical isotropic yield surface was postulated in strain space and the compliance tensor was used to transform it to a stress-based criterion.

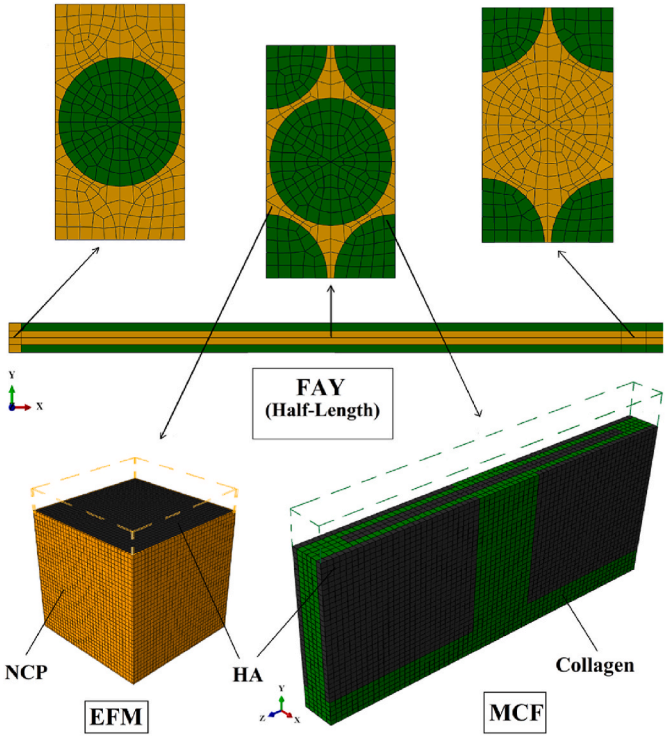

Fig. 2. Unit cell finite element model of bone ECM (Alizadeh et al., 2020).

Table 1
Elastic moduli (GPa) and Poisson's ratio of constituents in the FE model (Alizadeh et al., 2020).

Constituents	E_1	E_2	E_3	ϑ_{23}	ϑ_{31}	ϑ_{12}	G_{23}	G_{13}	G_{12}
MCF	12.98	12.98	30.91	0.12	0.28	0.23	4.17	4.17	5.25
EFM	25.34	25.34	25.34	0.08	0.08	0.08	4.44	4.44	4.44

Material identification is simplified by using an isotropic yield surface in strain space as only two independent material properties, including uniaxial tensile and compressive yield strains, are needed to define an anisotropic yield surface in stress space. A scalar function of the cumulated plastic strain (SDV) was used to illustrate the extent of plastic strain history in the material code. No damage, that is, no reduction of the elastic properties, was considered.

The use of an existing plasticity model for non-isotropic materials with a small number of material constants is an advantage of this approach.

Table 2 shows the yield properties of MCFs and EFMs, where ε_0^P and ε_0^N represent the uniaxial tensile and compressive yield strains, respectively.

2.3.1. Cohesive interfaces

To simulate the damage mechanism, including debonding and sliding between the MCF and EFM phases, the cohesive behavior in Abaqus was utilized. The cohesive interaction is formulated using a cohesive zone model (CZM) for simulating the fracture mechanism at the crack tip and traction-separation laws ahead of the crack tip, relating the process area opening displacement to the resisting tractions (Dugdale, 1960; Barenblatt, 1962).

The traction-separation model employed in the current study is plotted in Fig. 3a. The model consists of an initial linear elastic behavior which continues with damage initiation and damage evolution phases. The parameters t_{max} and δ_m° denote, respectively, the maximum values of contact traction and separation in purely normal or shear modes when damage and debonding are initiated. The δ_m^f parameter indicates the separation at final failure (Dassault Systems, 2014).

As provided in Eq. (1), the elastic stiffness tensor K relates the normal and shear tractions ($t_n, t_s, and\ t_t$) to the normal and shear separations (δ_n, $\delta_s, and\ \delta_t$) along the contact surfaces in the linear elastic phase.

Although the K matrix (Eq. (1)) characterizing a coupled relation between normal and shear tractions and separations consists of six terms due to its symmetry, several researchers (Chen and Teng, 2001; De Moura and Chousal, 2006; De Lorenzis et al., 2013; Park et al., 2016; Moslemi et al., 2020, 2021) indicate that the accuracy of the uncoupled form is sufficient. Thus, the non-diagonal components of K were assumed to be zero here.

$$t = \begin{Bmatrix} t_n \\ t_s \\ t_t \end{Bmatrix} = k\delta = \begin{bmatrix} K_{nn} & 0 & 0 \\ 0 & K_{ss} & 0 \\ 0 & 0 & K_{tt} \end{bmatrix} \begin{Bmatrix} \delta_n \\ \delta_s \\ \delta_t \end{Bmatrix} \tag{1}$$

In normal and shear modes, the bilinear traction-separation response (Fig. 3a) can be described by Eq. (2), where D_i is the damage variable.

$$t_i = \begin{cases} K_{ii}\delta_i, \delta_i \le \delta_m^{\circ} \\ (1 - D_i)K_{ii}\delta_i, \delta_m^{\circ} < \delta_i < \delta_m^f \\ 0\ ,\ \delta^f{}_m \le \delta_i \end{cases} \tag{2}$$

Table 2
Uniaxial yield strains in MCF and EFM.

Strain	Phases	
	MCF	EFM
ε_0^N	0.035	0.03
ε_0^P	0.023	0.02

Using the cohesive behavior model without the damage parameter leads to a linear elastic interaction. The damage item was added to the cohesive behavior in FE in the current study, including damage initiation and damage evolution (Hibbitt, 2013).

The maximum stress criterion was employed in which the damage is initiated in cohesive interfaces when the maximum contact ratio reaches the value of 1 (Eq. (3)). In Eq. (3), the peak value of contact stress, respectively, in normal and first or second shear directions, is designated by t_n°, t_s° and t_t° (Hibbitt, 2013). Only a positive, i.e. tensile normal traction can activate damage.

$$\max\left\{\frac{t_n}{t_n^{\circ}}, \frac{t_s}{t_s^{\circ}}, \frac{t_t}{t_t^{\circ}}\right\} \tag{3}$$

Then, the displacement criterion was used as a damage evolution factor to simulate the degradation in cohesive stiffness. Besides, in order to prevent penetration of elements in simulation, the hard contact model was used as a pressure-overclosure response in normal behavior (Fig. 3b) (Hibbitt, 2013; Dassault Systems, 2014).

As shown in Fig. 4, the MCF-EFM cohesive interactions were introduced between these two phases to simulate potential damage sites in the FAY model, and an MCF-MCF transverse interaction was defined at mid-length where the stresses are highest to include the possibility of MCF failure.

In finite element studies of ovine bone available in literature, the cohesive elements between constituents were applied and the electrostatic, water surface tension, van der Waals or viscous shear for normal and shear mode of cohesive elements were assumed (Hamed et al., 2010; Luo et al., 2011; Maghsoudi-Ganjeh et al., 2019; Xu and An, 2020) or the shear strength measured by Hang and Barber for antler bone (Hang and Barber, 2011; Wang and Ural, 2018a) was utilized in the simulation. It is noteworthy that in the current study, the FE model was used to simulate the fibril pull-out test performed by Hang et al. (Hang et al., 2014) on antler bone and the required shear properties in the cohesive interactions were compared with those experimental results (Hang et al., 2014) which fitted rather well with each other.

In current FE model, the K parameter was calculated by dividing the NCP's elastic modulus over its thickness (Eq. (4)). The NCP's elastic modulus ($E_{NCP} = 0.6\ GPa$) and thickness ($d_{NCP} = 0.24\ nm$) are derived from our previous two-scale modeling of bone ECM (Alizadeh et al., 2020). The strength in normal mode was fitted to the required debonding strength in cohesive interactions under tensile loading, and the ratio of shear strength to the normal strength was taken as the ratio of MCF's diameter to its length. The value of δ_m° was obtained by dividing the strength to stiffness (Eq. (1)) and the contact separation at final failure (δ_m^f) was assumed twice the contact separation when debonding is initiated (δ_m°). The material properties used in cohesive interfaces in this study including, t, and the corresponding δ_m° are presented in Table 3 revealing for the first time the stiffness, normal and shear strength, and contact separation of interfaces for ovine bone at lamellar level. The shear strength in the current study was almost 3.5 MPa, which is in the (broad) shear strength range (0.6–64 MPa) of cohesive elements used in other studies (Luo et al., 2011; Hamed and Jasiuk, 2013; Hang et al., 2014; De Falco et al., 2017; Lai and Yan, 2017; Wang and Ural, 2018b, 2019; Maghsoudi-Ganjeh et al., 2019; Xu and An, 2020).

$$K = \frac{E_{NCP}}{t_{NCP}} = 2.5\ \frac{N}{\mu m^3} \tag{4}$$

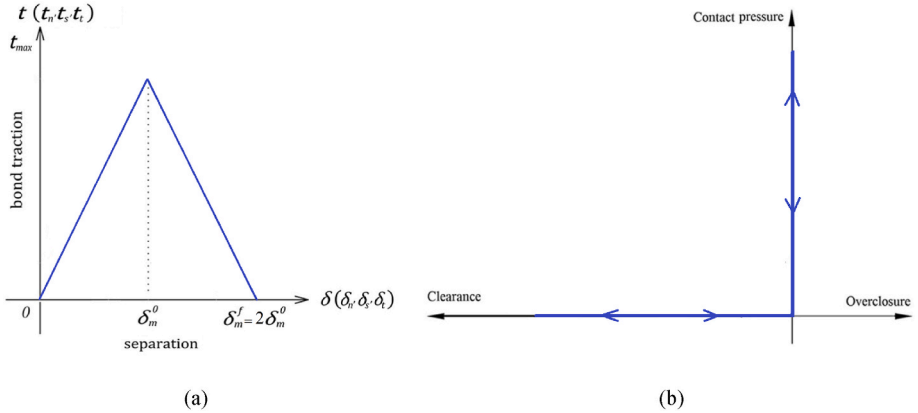

Fig. 3. Contact behavior used in FEM (a)Traction-separation behavior, (b) Hard contact pressure-overclosure contact response (Dassault Systems, 2014).

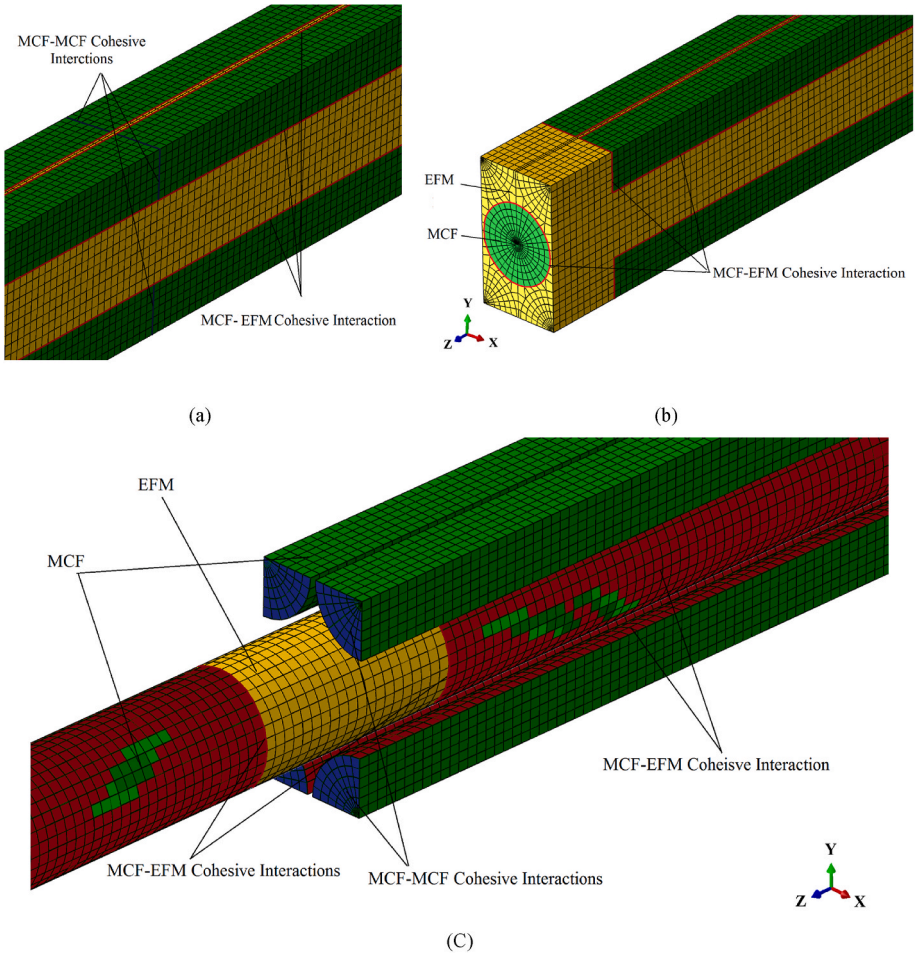

Fig. 4. Cohesive interactions in FE model of bone ECM, (a) longitudinal MCF-EFM interactions and transverse MCF-MCF interaction at the middle part of FAY, (b) longitudinal and transverse MCF-EFM interactions at the end part of FAY, (c) Interfaces in the gap zone inside the model at middle part of length after removing the external EFM constituent (In current FE model, the interfaces at the ends of the central MCF were ignored).

2.4. Periodic boundary condition

In order to reduce the numerical simulation costs, a representative volume element (RVE) in the form of a unit cell with periodic boundary conditions (PBC) was employed, and four different loading cases, including tensile and compressive load in axial and transverse directions, were applied in four analyses. The description of the utilized PBC code is provided in Appendix A.

3. Results

3.1. Stress-strain results of bone ECM under tensile and compressive loading

The FE stress-strain results of bone ECM under tensile and compressive loading in axial and transverse directions are presented in Fig. 5, in which the bone ECM shows brittle behavior under tensile axial

Table 3
Material data used in modeling the cohesive interfaces (the contact separation (δ_m°) presented in the table is calculated based on Eq. (1) using K and t parameters).

Interactions	Fracture Mode	K ($\frac{N}{\mu m^3}$)	t (GPa)	δ_m° (μm)
MCF-MCF	Normal mode (I)	2.5	3.8×10^{-1}	1.52×10^{-4}
	Shear mode (II)	2.5	3.8×10^{-3}	1.52×10^{-6}
MCF-EFM	Normal mode (I)	2.5	3.5×10^{-1}	1.40×10^{-4}
	Shear mode (II)	2.5	3.5×10^{-3}	1.40×10^{-6}

and transverse loading and ductile behavior under compressive loading in both axial and transverse directions.

The simulation results of tensile axial loading (Fig. 5a) indicate that the stress–strain curve started with an initial linear response. Stretching the FAY causes interfacial shear and debonding damage between MCF and EFM, and as the applied strain increases, the stress reaches its maximum strength (~0.35 GPa) at around 1.36% strain. Thereafter, the stress gradually dropped to 0.05 GPa ($\varepsilon_{33} = 1.38\%$) because of multiple damage patterns (e.g., sliding and interface debonding) showing the load transfer from MCF to EFM. The final failure of bone ECM under tensile axial loading was fibril failure at mid-length and fibril pull-out.

The model-predicted stress-strain curve under transverse tensile loading (Fig. 5b) was initiated with a linear elastic behavior, and after increasing the applied strain, the interfacial damage began to start and evolve in the model. The stress peaked at ~0.136 GPa at $\varepsilon_{11} = 1.05\%$ and then fell to 0.02 GPa due to the debonding between the MCF-EFM phases.

The simulation results of FAY under compressive loading and unloading (Fig. 5c and d) showed a linear elastic response at the start of the stress-strain curve, and as the strain increased, sliding between MCF-EFM constituents occurred, and the stress-strain curve yielded followed by a perfect plasticity response.

The stress-strain results of numerical simulation under tensile loading and compressive loading/unloading are compared with experimental results (Schwiedrzik et al., 2014; Casari et al., 2021) (Fig. 5), and the ultimate strength and the stress-strain behavior obtained from simulation results matched well with those from the experiments. The elastic modulus difference between numerical and experimental results is due to visco and poroelasticity, which are not included in our numerical simulations. Indeed, the higher elastic modulus in FE result in comparison with experimental results is due to the instantaneous or undrained elastic modulus used in FE models.

3.2. Mechanical behavior of FAY under tensile loading

3.2.1. Axial tensile loading stress distribution and failure mechanism

This section discusses the stress distribution and failure mechanisms of bone ECM under axial tensile loading, such as progressive failure of cohesive interactions, sliding and debonding between MCF and EFM constituents, fibril pull-out and fibril failure.

The damage evolution in cohesive interactions is shown with the scalar stiffness degradation for cohesive surfaces (CSDMG) under axial tensile loading at different strains (Fig. 6). The cohesive interface damage criterion (CSDMG) shifts from zero (blue) to one (red), revealing both undamaged interfaces and complete failure in cohesive interactions, respectively.

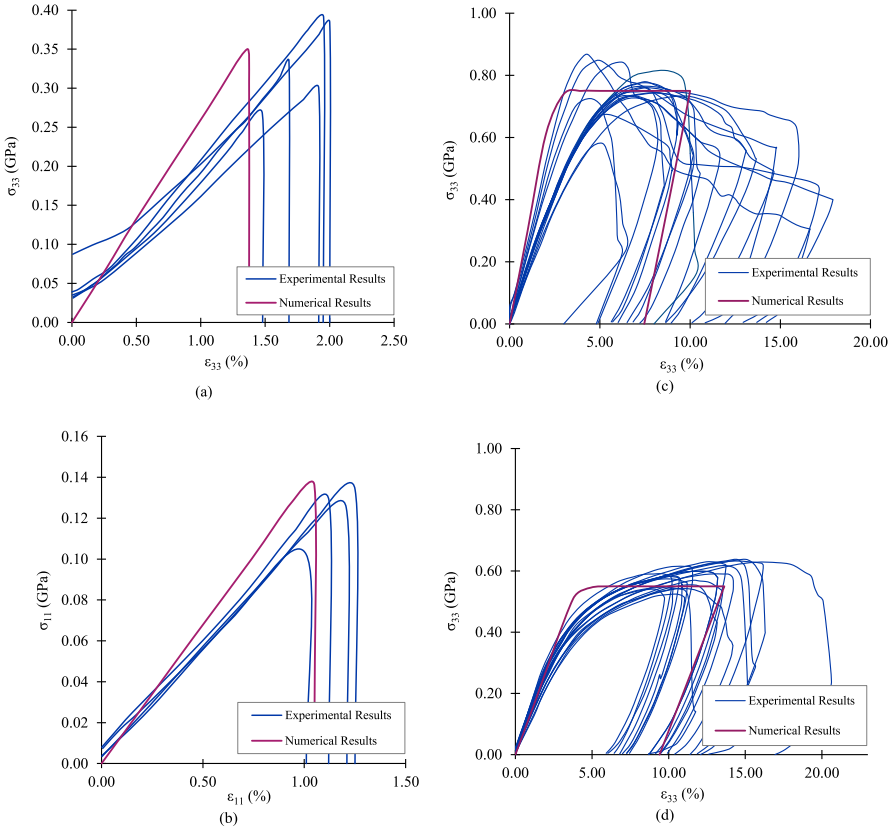

Fig. 5. Numerical results under tensile loading and compressive loading/unloading and experimental results of bone ECM, (a) axial tensile, (b) transverse tensile, (c) axial compression, (d) transverse compression (The difference between elastic modulus in numerical and experimental results is due to the visco- and poroelasticity which is not included in numerical analysis) (Schwiedrzik et al., 2014; Casari et al., 2021).

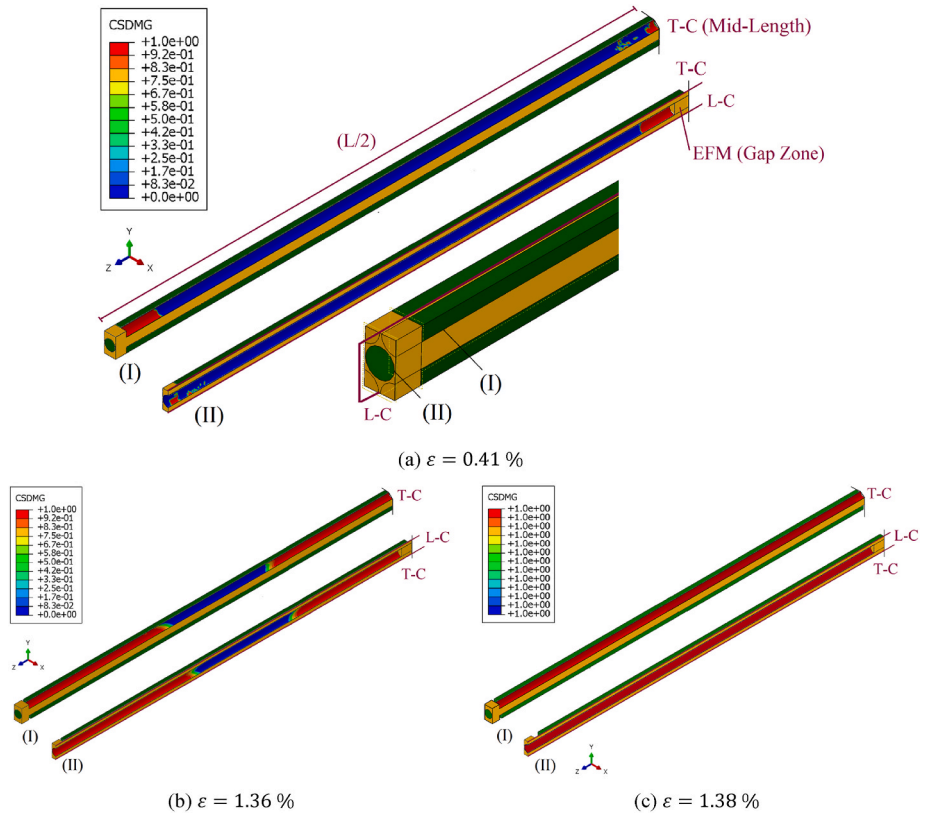

Fig. 6. Damage propagation (CSDMG) at corner and central MCF-EFM cohesive interactions of FAY under axial tensile loading (Z direction) at different applied strains, (a) $\varepsilon = 0.41$ % , (b) $\varepsilon = 1.36$ %, (c) $\varepsilon = 1.37$ % (only half-length of the FAY is shown due to symmetry).

Due to the symmetry of the damage mechanism in cohesive interactions, only the half-length of the fibril array is shown in Fig. 6 (FAY is cut in the transverse direction at the middle part of the length (T-C)) under three strain values, including 0.41, 1.36 (peak load) and 1.38 percent (complete failure). For each strain level, two FAY models show the cohesive interfaces at the corner of FAY by removing the MCF at the corner (6 a-I, b-I, c-I), and at the central part of FAY (6 a-II, b-II, c-II), by removing the central MCF and cutting the FAY in the longitudinal direction (L-C), in addition to the transverse cut in the middle of FAY (T-C).

The failure mechanism in cohesive interfaces was initiated simultaneously at the ends and at the middle of the FAY and propagated through the length with increasing strains. As shown in Fig. 7, the longitudinal interfaces (MCF-EFM interactions) and transverse MCF-EFM and MCF-

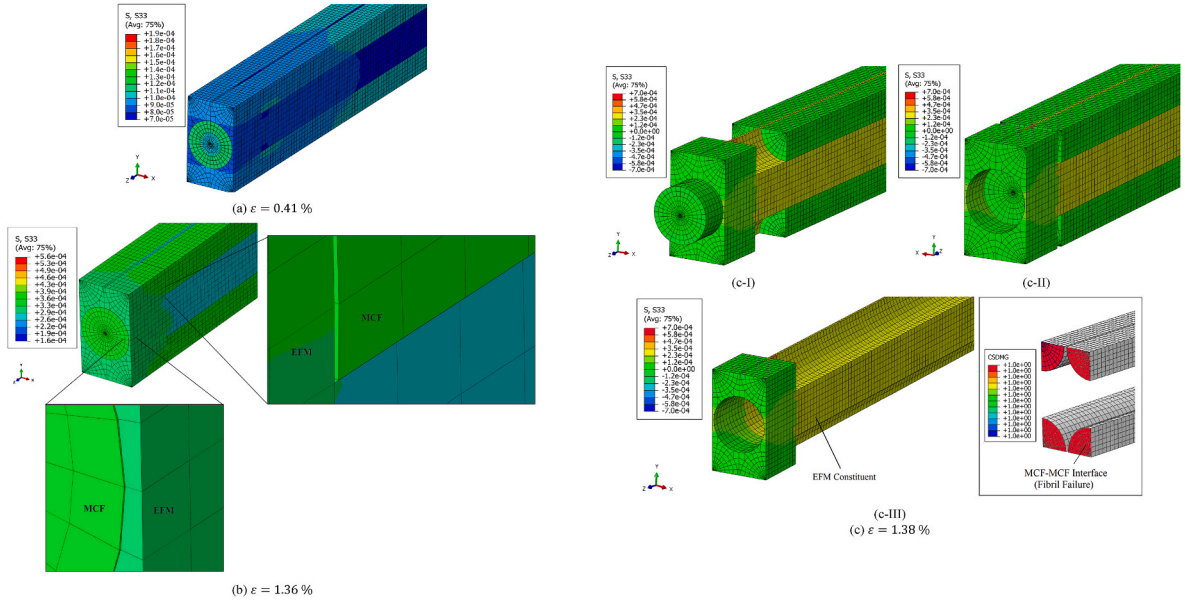

Fig. 7. Stress distribution and failure mode of FAY at different applied strains under axial tensile loading (Z direction), (a) = 0.41 % , (b) $\varepsilon = 1.36$ %, (c) $\varepsilon = 1.37$ % ((C–I), (C-II) Fibril pull-out and sliding at two ends, (C-III) EFM part and MCF-MCF interface failure (Unit: $\frac{N}{\mu m^2}$).

MCF interactions were completely debonded, allowing for fibril pull-out at maximum strain.

Fig. 7 depicts the stress distribution and damage mechanism of FAY under axial tensile load, including longitudinal sliding and fibril pull-out at two ends, fibril debonding inside the model, and fibril failure due to MCF-MCF interaction damage.

During the pre-yield deformation (at a low value of strain), the axial tensile stresses in MCF were higher than in EFM, indicating that MCF was the primary load-sustaining constituent and the sliding between MCF and EFM constituents started under loading (Fig. 7a). As the model was further stretched, the sliding between fiber and matrix was propagated and the traction in the transverse cohesive interactions (MCF-EFM and MCF-MCF) reached the critical strength. Following that, the separation in cohesive interfaces exceeded the failure separation, and debonding between MCF and EFM occurred at 1.36 (Fig. 7b), with the axial normal load still primarily sustained by the MCF. As axial strain increased, the damage in MCF-EFM longitudinal interaction propagated through the full length (Fig. 6c), leading to fibril pull out, and eventually, the overall failure of the model occurred (Fig. 7c). Following fibril pull-out, the central MCF moved to the outside and the inside of the FAY at the two ends (as shown in Fig. 7c–I and c-II). Besides, the fibril failure occurred in the middle part of FAY during the loading process and the damage criterion in MCF-MCF cohesive interactions reached its maximum value as presented in Fig. 7c–III. It is worth noting that load was gradually transferred to the remaining EFM during the post-yield deformation (Fig. 7c–III).

The experimental results of bone ECM (Casari et al., 2021) indicated that the MCF-EFM interfaces shear failure and fibril pull out occurred under tensile axial loading, which is reflected in our numerical results at this stage.

3.2.2. Transverse tensile loading stress distribution and failure mechanism

Using the CSDMG criterion, the damage evolution in cohesive interfaces under transverse tensile loading at different applied strains is presented in Fig. 8. The status of the ends and the central cohesive interfaces are shown at each strain level by providing two FAY representations, which are both cut at the middle due to symmetry.

In order to demonstrate the progressive failure in the interfaces, the MCF part at the corner is removed from the FAY model as shown in Fig. 8a–I, b-I, the central MCF is separated from the FAY model in Fig. 8a–II, b-II, and the model is cut in the longitudinal direction (L-C). Fig. 8a–b shows that the damage mechanism in visible interfaces was initiated from the top (normal) surface of the MCF and propagated to the bottom (tangent) surface due to normal loading in the transverse direction, which occurred in all longitudinal interfaces of FAY due to symmetry.

Fig. 8b–I reveals that the damage mechanism in the interfaces tends to progress from the middle towards the ends, and there is still weak adhesion in some sites along the length.

Stress distribution and fibril-matrix debonding under transverse tensile loading at the corner and middle part of FAY are shown in Fig. 9a and b, respectively. Transverse normalstress in EFM was higher than that of MCF subunits due to MCF debonding, showing that EFM was the load-carrying constituent. The stress concentration in FAY, which is shown at the ends and in the middle, is due to the transverse continuity of EFM constituents located in the gap regions.

Because of the transverse normal loading in FAY, traction in the cohesive elements at several parts of the MCF-EFM interfaces reached critical strength, and cohesive damage was initiated (Fig. 9) and evolved in those MCF-EFM interfaces. Further stretching of the model caused the interfaces between adjacent MCF and EFM subunits to undergo separation and eventually resulted in delamination between the two constituents. As reported in the recent micro-tensile test (Casari et al., 2021), delamination between EFM and MCF caused the FE model to fail under transverse tensile loading.

3.3. Mechanical behavior of FAY under compressive loading

3.3.1. Axial compressive loading stress distribution and failure mechanism

The stress distribution of FAY under axial compressive loading at the end and middle part is shown in Fig. 10, and the cumulated plastic strains (SDV1) under the two applied strains is given in Fig. 11.

As shown in Fig. 10, the higher stresses in the MCF compared to the EFM phase confirm that the axial load is mainly sustained by the MCF (the blue to red colors in the plot show the highest to the lowest values of stresses) and Fig. 11 indicates the almost similar cumulated plastic

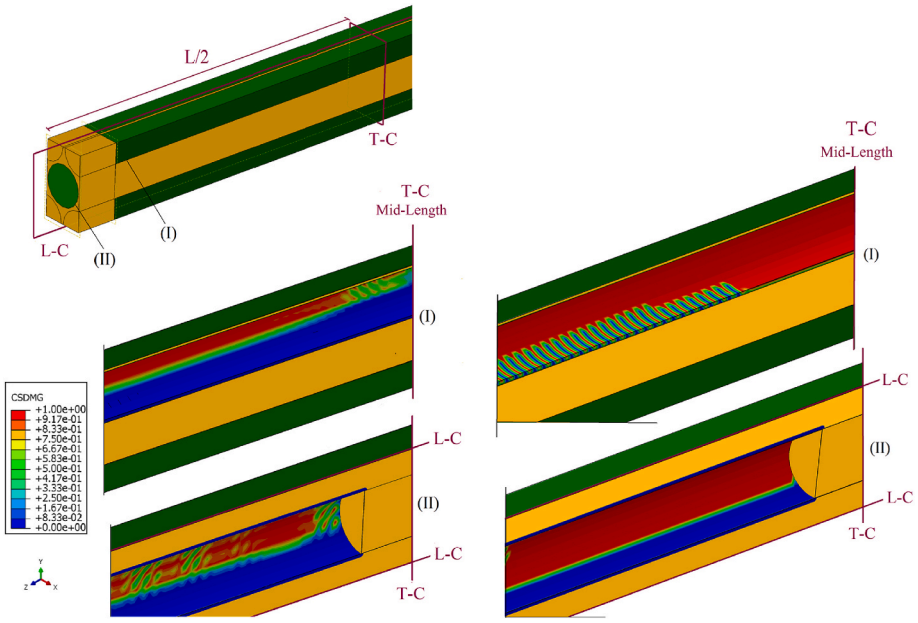

Fig. 8. Damage propagation (CSDMG) at the end and in the central MCF-EFM cohesive interactions of FAY under transverse tensile loading (X direction) at different applied strains, (a) $\varepsilon = 0.50$ % , (b) $\varepsilon = 1.05$ % (the FAY model is cut in the middle due to symmetry).

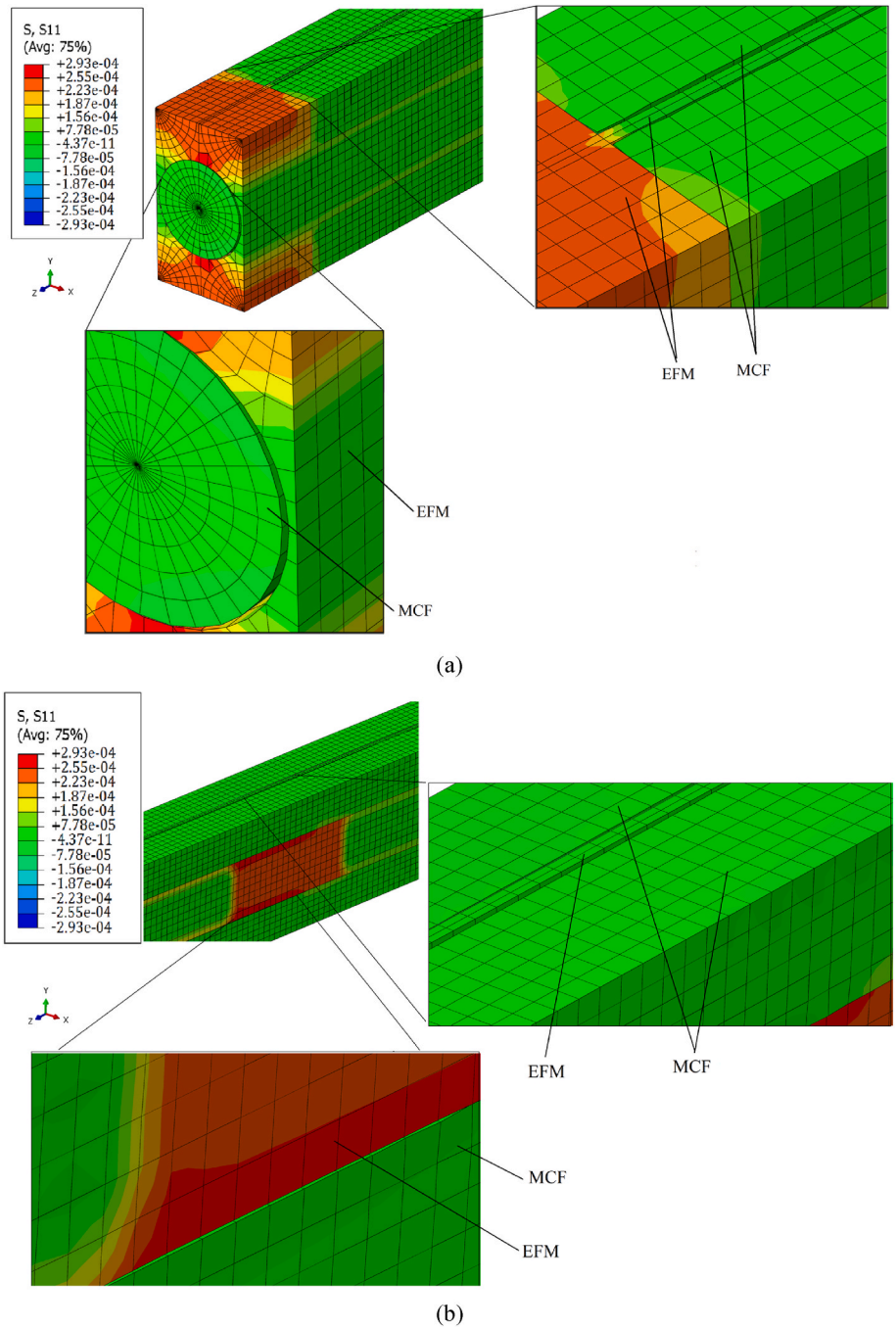

Fig. 9. Stress distribution and MCF-EFM debonding in FAY under transverse tensile loading (x direction), (a) at the end and (b) in the middle of the FAY (Unit: $\frac{N}{\mu m^2}$).

strains in the MCF and EFM phases under axial compressive loading. The numerical results of the FAY model under axial compressive loading (Figs. 10 and 11) reveal the plasticity and MCF-EFM sliding, which are compatible with experimental results reported in the micropillar compression test of ovine lamellar bone (Schwiedrzik et al., 2014).

3.3.2. Transverse compressive loading stress distribution and failure mechanism

The stress distribution of FAY under transverse compressive loading is shown in Fig. 12, and the cumulated plastic strains under two strain levels are shown in Fig. 13. The numerical results show that the EFM is the load-bearing phase under transverse compressive loading, and the plasticity appearing in the model fits with experimental results of micropillar compression tests in the transverse direction (Schwiedrzik et al., 2014). The higher value of cumulated plastic strains in the MCF constituent is most likely due to the lower stiffness of transversely isotropic MCF material in the transverse direction compared with the isotropic EFM phase (Fig. 13).

4. Discussion and conclusion

The aim of this study was to develop an efficient FE model of a uniaxial mineralized collagen fibril array (FAY) to represent its load transfer, post-yield behavior, and failure mechanism under tensile and compressive loading in both axial and transverse directions. As a result, our 3D unit-cell FE model of FAY calibrated for linear elasticity (Alizadeh et al., 2020) was equipped with cohesive interactions and plasticity constitutive models to simulate the anisotropic post-yield properties of

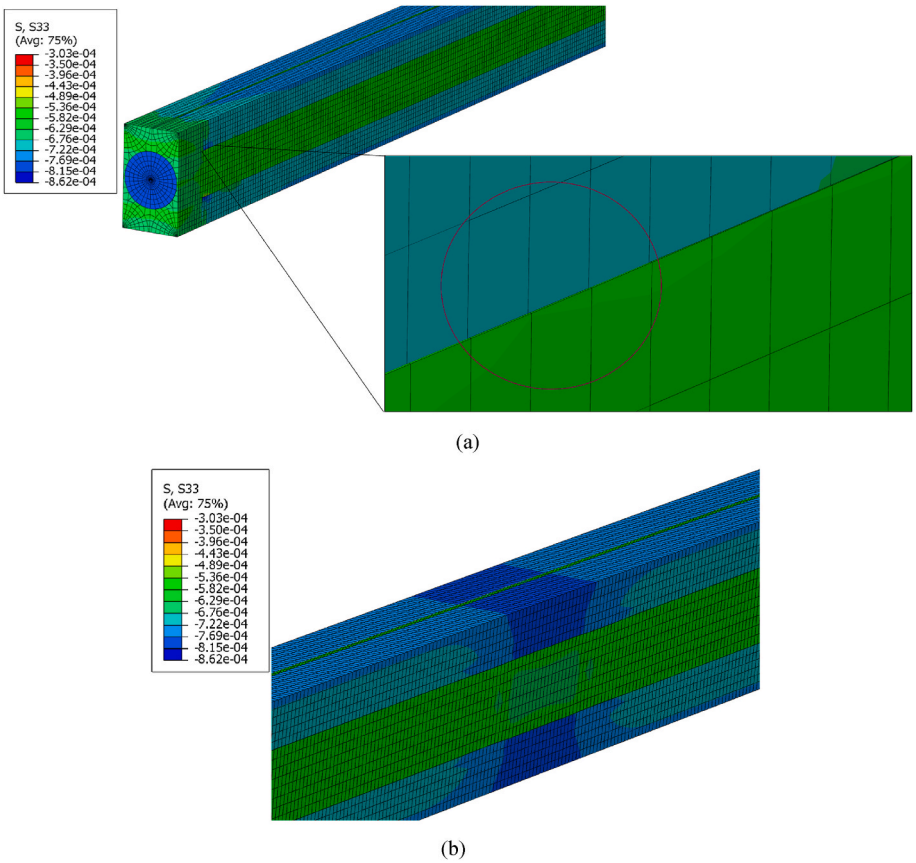

Fig. 10. Stress distribution and MCF-EFM debonding in FAY under axial compressive loading (Z direction), (a) at the end, (b) at the middle of the FAY (Unit: $\frac{N}{\mu m^2}$) (the blue color shows the highest stress intensity).

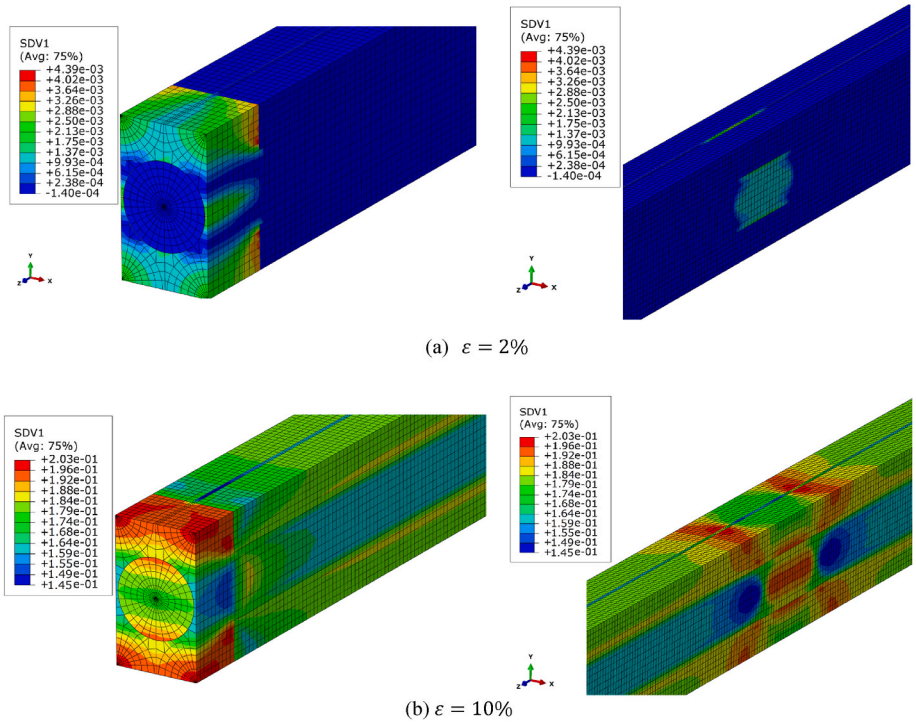

Fig. 11. Cumulated plastic strains (SDV1) in FAY under axial compressive loading (Z direction) at the end and the middle of the FAY under different strain levels, (a) 2% , (b) 10% (Unit: $\frac{N}{\mu m^2}$).

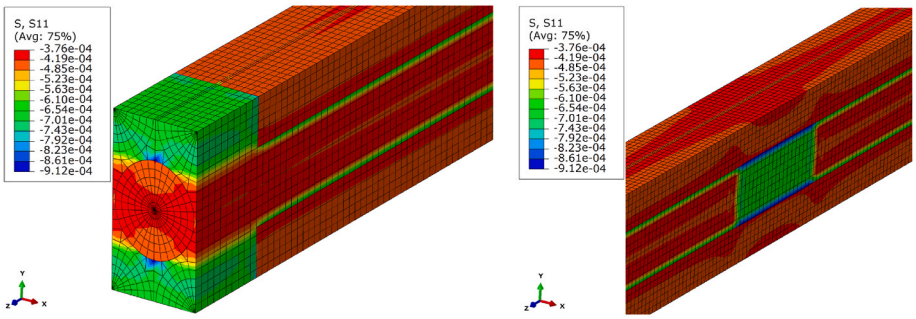

Fig. 12. Stress distribution in FAY under transverse compressive loading (Z direction), (a) at end part, (b) at middle part of FAY (Unit: $\frac{N}{\mu m^2}$) (the blue color shows the highest stress intensity).

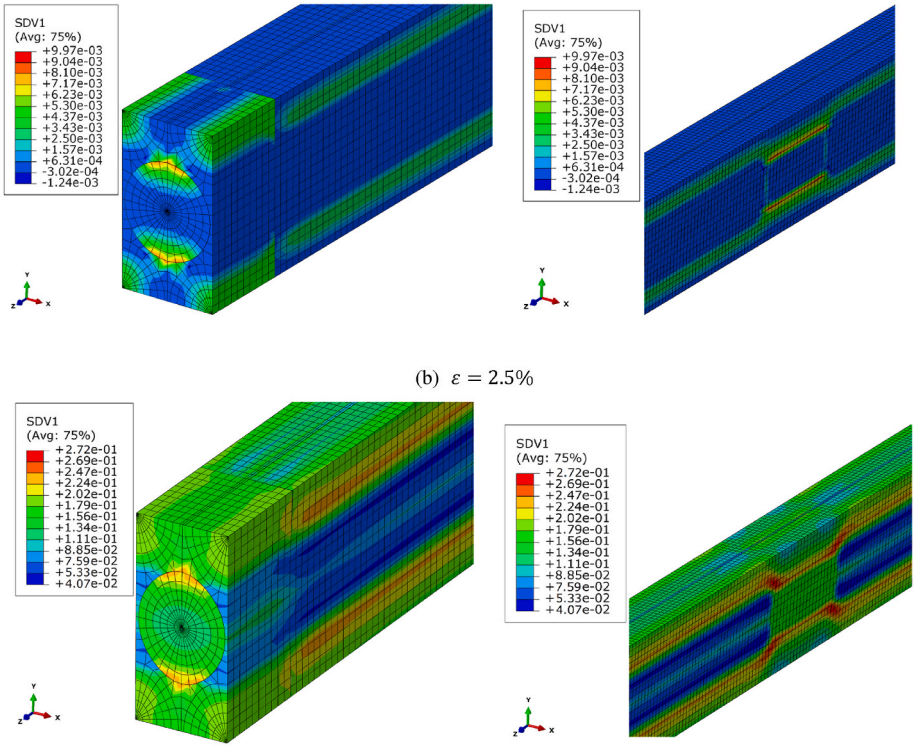

Fig. 13. Cumulated plastic strains (SDV1) in FAY under transverse compressive loading (Z direction) at the end and the middle of the FAY under different strain levels, (a) 2.5% , (b) 13% (Unit: $\frac{N}{\mu m^2}$).

the FAY recently measured by micropillar compression (Schwiedrzik et al., 2014) and micro-tensile tests (Schwiedrzik et al., 2014), (Casari et al., 2021).

According to the reported failure mechanisms in these experimental investigations, the damage in axial tensile loading (Casari et al., 2021) occurs in shear at the MCF/EFM interfaces, leads to fibril pull-out, results in brittle failure, and a rough and porous fracture surface. In tensile transverse loading (Casari et al., 2021), failure also occurred at the MCF-EFM interface but in a mixed normal and shear mode. Micropillar compression tests, on the other hand, revealed a plastic onset followed by MCF-EFM interface failure at higher strains in both the axial and transverse loading directions (Schwiedrzik et al., 2014).

Damage accumulation and strength of our unit-cell FAY finite element model (Alizadeh et al., 2020) were evaluated by using cohesive interactions between MCF and EFM and in a transverse plane at the central part of the MCF. The mechanical properties of cohesive interactions between constituents of ovine bone ECM were calculated here for the first time by using our previous study (Alizadeh et al., 2020) and calibrating our current FE model with experimental results (Schwiedrzik et al., 2014; Casari et al., 2021). Using a custom UMAT (Schwiedrzik and Zysset, 2013) to define plasticity in the model, isotropic yield strain was assumed in the EFM and MCF, and thus transversely isotropic yield strength in the MCF.

The non-linear bone FAY model was investigated, and the FAY FE stress-strain curves were compared with micropillar and micro-tensile tests (Schwiedrzik et al., 2014; Casari et al., 2021), which matched well with the individual experiments in both axial and transverse directions, indicating brittle and ductile behavior for tensile and compressive loading, respectively. In addition to the similarity between stress-strain results predicted by the FE simulation and those obtained by the experiment, the failure mechanisms of our model are also in good agreement with the experimental observations. The finite element

results in the current study indicated that under axial tensile loading, shear failure in MCF-EFM interaction was initiated at the load transfer zones between MCF and EFM and fibril failure occurred where maximal stress appeared in the MCF. As the applied load increased, the shear failure eventually developed throughout the entire length, leading to fibril pull-out failure. The damage mechanism, including debonding and sliding, prevents the load transfer from MCF to EFM in FAY to sustain tensile axial loading. Furthermore, normal failure in MCF-EFM interfaces and debonding between MCF and EFM occurred under transverse tensile loading, causing the brittle behavior of bone ECM. Indeed, the predicted FE models could improve the detailed understanding of how and where progressive damage formation occurs under tensile loading.

Another evidence which supports the presented FE model is the good agreement between simulation prediction and experimental observation (Schwiedrzik et al., 2014) in compressive loading, indicating the plasticity, ductile behavior, and sliding between MCF and EFM layers in axial and transverse directions. The unloading curves of compressive simulation demonstrated perfect plasticity without significant reduction of elastic modulus and consequently damage in the FE unit-cell model corresponding to the micropillar compression test (Schwiedrzik et al., 2014) in which the single bone lamellae showed high strength and ductility but no damage. In fact, damage appears at a higher scale of bone under compressive loading through stress concentration around heterogeneities. Under compressive loading, the macroscopic response of bone containing several osteons reveals significant damage and cracks with lower strength and ductility when compared to the bone lamellar level (Schwiedrzik et al., 2014).

Indeed, the strength and failure mechanism of bone ECM under tensile and compressive loading in both axial and transverse directions reproduced the experimental observations and provided the average bone material parameters at this scale.

Although the mechanical behavior of bone captured using our FE model is consistent with the experimental studies, it has some limitations. A 3D unit-cell model was used with periodic boundary conditions to simulate efficiently a mean nonlinear response of bone ECM under different loading cases. However, this approach does not account for the statistical distribution of the geometrical features and material properties. The cylinders with transversal cohesive surfaces were used to model the MCFs and interactions between two phases in FAY leading to some limitations in modeling the failure mechanism compared to the more realistic conical shape of the mineralized collagen fibrils. Viscoelasticity and poroelasticity were not modeled in the current work and the plasticity model without damage and a low number of material constants was used, which reproduces properly the behavior of FAY compared with experimental results (Schwiedrzik et al., 2014). It is difficult to determine the cohesive interface properties of bone ECM using independent experimental tests, and those values were calculated for ovine bone based on calibrating our FE model with the experiments (Schwiedrzik et al., 2014; Casari et al., 2021).

The 3D FE model of bone at the lamellar level presented here reproduced for the first time the post-yield behavior, failure mechanism, and strength tension-compression asymmetry of bone under both axial and transverse loading cases of state-of-the-art micro pillar compression and micro-tensile experimental results (Schwiedrzik et al., 2014; Casari et al., 2021). The proposed FE model could be exploited as an input for the investigation of the post-yield properties of various architectures of lamellar bone (Razi et al., 2020), and ultimately, the mesoscopic post-yield behavior of compact and trabecular bone could be derived. Clarifying the relationships between multi-scale bone organization and macroscopic strength will help refining the diagnosis of bone fragility, improving primary stability of implants in bone and contributing to the design of novel biomimetic materials.

CRediT authorship contribution statement

Elham Alizadeh: Writing – review & editing, Writing – original draft, Visualization, Validation, Methodology, Investigation, Formal analysis, Data curation. **Sadik Omairey:** Writing – review & editing, Resources. **Philippe Zysset:** Writing – review & editing, Validation, Supervision, Resources, Project administration, Methodology, Conceptualization.

Declaration of competing interest

The authors declare that they have no known competing financial interests or personal relationships that could have appeared to influence the work reported in this paper.

Data availability

Data will be made available on request.

Acknowledgment

This study was funded by the Swiss Government Excellence Scholarship, Grant/Award Number (2021.0686).

Appendix A

The unit-cell models with PBC were used in the current study in which the aim was to use the standard EasyPBC homogenization tool in ABAQUS FEA software (Omairey et al., 2019) to estimate the strength and failure mechanism of the modeled RVEs as it offers the freedom to create a wider range of geometries in the pre-processing and extended access to the post-processing analysis data. The EasyPBC tool implements homogenization by numerically imposing uniform strains and deformations on the RVE to obtain the overall engineering moduli. However, the current version of EasyPBC is limited to analyzing RVEs that consist of a single assembly instance; in other words, RVE phases must be analyzed as fully connected interfaces. Given the fact that one of the objectives of this study is investigating the interface behavior between the different phases, EasyPBC has been developed further to allow the analysis of multiple instances, in this case, MCFs and EFM phases. To achieve this, the following changes were implemented:

The code is amended to search for the different boundary surfaces of the RVE in all existing instances rather than the pre-defined instance in the stranded version of the plugin. This also included changes to how each node set's information is stored, namely the inclusion of instance name along with node label as labelling number restarts from 1 for each instance. This is necessary to ensure that nodes have corresponded correctly.

In the standard code, the generated node sets are sorted to facilitate the linking of nodal degrees of freedom to implement PBCs. To achieve this, for each node in associated sets/pairs, the code identifies its corresponding node in the opposite set when the coordinate difference between the two nodes is smaller than a specified mapping accuracy. Once a pair of nodes is found, both are appended in the same order in their sets. However, given that there are multiple instances in this study, interface nodes at the boundaries of the RVE can have the same coordinate yet belong to different instances; Therefore, an additional condition is added to ensure that opposite nodes are linked when the material of the instances match, shown in Fig. 14. To aid the matching algorithm, instances are named with distinct "MCF" and "EFM" wording.

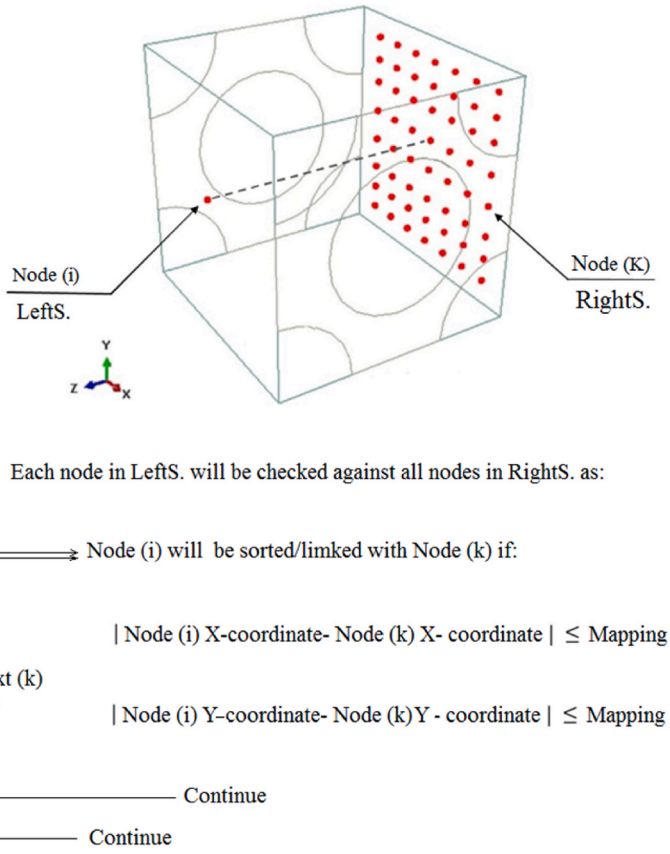

Fig. 14. Mechanism used to add nodes within associated sets (Omairey et al., 2019).

References

Alizadeh, E., Dehestani, M., Zysset, P., 2020. An efficient two-scale 3D FE model of the bone fibril array: comparison of anisotropic elastic properties with analytical methods and micro-sample testing. Biomech. Model. Mechanobiol. 19 (6), 2127–2147.

An, B., Li, Y., 2021. Role of strain rate sensitivity of extrafibrillar matrix on fracture in mineralized collagen fibril arrays. Eng. Fract. Mech. 245, 107592.

Aoubiza, B., Crolet, J.M., Meunier, A., 1996. On the mechanical characterization of compact bone structure using the homogenization theory. J. Biomech. 29 (12), 1539–1547.

Barenblatt, G.I., 1962. The mathematical theory of equilibrium cracks in brittle fracture. Adv. Appl. Mech. 7, 55–129.

Barkaoui, A., et al., 2014. Multiscale approach including microfibril scale to assess elastic constants of cortical bone based on neural network computation and homogenization method. Intern. J. Numerical Method. Biomed. Eng. 30 (3), 318–338.

Barkaoui, A., Bettamer, A., Hambli, R., 2011. Mechanical behaviour of single mineralized collagen fibril using finite element simulation coupled to quasi-brittle damage law. In: European Congress on Computational Methods in Applied Sciences and Engineering. ECCOMAS 2012, p. 9.

Barkaoui, A., Hambli, R., 2011. Finite element 3D modeling of mechanical behavior of mineralized collagen microfibrils. J. Appl. Biomater. Biomech. 9 (3), 199–206.

Budiansky, B., 1965. On the elastic moduli of some heterogeneous materials. J. Mech. Phys. Solid. 13 (4), 223–227.

Buehler, M.J., 2007. Molecular nanomechanics of nascent bone: fibrillar toughening by mineralization. Nanotechnology 18 (29), 295102.

Casari, D., et al., 2019. A self-aligning microtensile setup: application to single-crystal GaAs microscale tension–compression asymmetry. J. Mater. Res. 34 (14), 2517–2534.

Casari, D., et al., 2021. Microtensile properties and failure mechanisms of cortical bone at the lamellar level. Acta Biomater. 120, 135–145.

Chen, J.F., Teng, J.G., 2001. Anchorage strength models for FRP and steel plates bonded to concrete. J. Struct. Eng. 127 (7), 784–791.

Currey, J.D., 2013. Bones, in Bones. Princeton University Press.

Dassault Systems, F., 2014. 'Abaqus Analysis User's Guide (6.14)'. Abaqus FEA, Providence, Rhode Island.

Dong, X.N., Guo, X.E., 2006. Prediction of Cortical Bone Elastic Constants by a Two-Level Micromechanical Model Using a Generalized Self-Consistent Method.

De Falco, P., et al., 2017. Staggered fibrils and damageable interfaces lead concurrently and independently to hysteretic energy absorption and inhomogeneous strain fields in cyclically loaded antler bone. ACS Biomater. Sci. Eng. 3 (11), 2779–2787.

Dugdale, D.S., 1960. Yielding of steel sheets containing slits. J. Mech. Phys. Solid. 8 (2), 100–104.

Fantner, G.E., et al., 2005. Sacrificial bonds and hidden length dissipate energy as mineralized fibrils separate during bone fracture. Nat. Mater. 4 (8), 612–616.

Fratzl, P., Weinkamer, R., 2007. Nature's hierarchical materials. Prog. Mater. Sci. 52 (8), 1263–1334.

Fritsch, A., Hellmich, C., 2007. Universal'microstructural patterns in cortical and trabecular, extracellular and extravascular bone materials: micromechanics-based prediction of anisotropic elasticity. J. Theor. Biol. 244 (4), 597–620.

Hambli, R., Barkaoui, A., 2012. Physically based 3D finite element model of a single mineralized collagen microfibril. J. Theor. Biol. 301, 28–41.

Hamed, E., Jasiuk, I., 2013. Multiscale damage and strength of lamellar bone modeled by cohesive finite elements. J. Mech. Behav. Biomed. Mater. 28, 94–110.

Hamed, E., Lee, Y., Jasiuk, I., 2010. Multiscale modeling of elastic properties of cortical bone. Acta Mech. 213 (1), 131–154.

Hang, F., Barber, A.H., 2011. Nano-mechanical properties of individual mineralized collagen fibrils from bone tissue. J. R. Soc. Interface 8 (57), 500–505.

Hang, F., Gupta, H.S., Barber, A.H., 2014. Nanointerfacial strength between non-collagenous protein and collagen fibrils in antler bone. J. R. Soc. Interface 11 (92), 20130993.

Hassenkam, T., et al., 2004. High-resolution AFM imaging of intact and fractured trabecular bone. Bone 35 (1), 4–10.

Hibbitt, K., 2013. 'ABAQUS: User's Manual: Version 6.13. Hibbitt', USA (Karlsson & Sorensen).

Hill, R., 1963. Elastic properties of reinforced solids: some theoretical principles. J. Mech. Phys. Solid. 11 (5), 357–372.

Jasiuk, I., Ostoja-Starzewski, M., 2004. Modeling of bone at a single lamella level. Biomech. Model. Mechanobiol. 3 (2), 67–74.

Lai, Z.B., Yan, C., 2017. Mechanical behaviour of staggered array of mineralised collagen fibrils in protein matrix: effects of fibril dimensions and failure energy in protein matrix. J. Mech. Behav. Biomed. Mater. 65, 236–247.

De Lorenzis, L., Fernando, D., Teng, J.-G., 2013. Coupled mixed-mode cohesive zone modeling of interfacial debonding in simply supported plated beams. Int. J. Solid Struct. 50 (14–15), 2477–2494.

Luo, Q., et al., 2011. Effect of mineral–collagen interfacial behavior on the microdamage progression in bone using a probabilistic cohesive finite element model. J. Mech. Behav. Biomed. Mater. 4 (7), 943–952.
Ma, Z., et al., 2021. Disparate micro-mechanical behaviors of adjacent bone lamellae through in situ SEM micropillar compression. Mater. Sci. Eng., A 825, 141903.
Maghsoudi-Ganjeh, M., et al., 2019. Computational investigation of ultrastructural behavior of bone using a cohesive finite element approach. Biomech. Model. Mechanobiol. 18 (2), 463–478.
Mori, T., Tanaka, K., 1973. Average stress in matrix and average elastic energy of materials with misfitting inclusions. Acta Metall. 21 (5), 571–574.
Moslemi, A., et al., 2020. Proposing and finite element analysis of a new composite profiled sheet deck. In: Structures, pp. 70–85.
Moslemi, A., et al., 2021. Numerical investigation of post-tensioned concrete slab developed by hybrid concrete, PU foams, PVC, and GFRP. Internation. J. Advan. Eng. Sci. Appl. Math. 1–16.
De Moura, M., Chousal, J.A.G., 2006. Cohesive and continuum damage models applied to fracture characterization of bonded joints. Int. J. Mech. Sci. 48 (5), 493–503.
Nair, A.K., et al., 2013. Molecular mechanics of mineralized collagen fibrils in bone. Nat. Commun. 4 (1), 1–9.
Nikel, O., Poundarik, AA., Bailey, S., Vashishth, D., 2018. Structural role of osteocalcin and osteopontin in energy dissipation in bone.J. Biomech 80, 45–52.
Nikolov, S., Raabe, D., 2008. Hierarchical modeling of the elastic properties of bone at submicron scales: the role of extrafibrillar mineralization. Biophys. J. 94 (11), 4220–4232.
Olszta, M.J., et al., 2007. Bone structure and formation: a new perspective. Mater. Sci. Eng. R Rep. 58 (3–5), 77–116.
Omairey, S.L., Dunning, P.D., Sriramula, S., 2019. Development of an ABAQUS plugin tool for periodic RVE homogenisation. Eng. Comput. 35 (2), 567–577.
Park, K., Choi, H., Paulino, G.H., 2016. Assessment of cohesive traction-separation relationships in ABAQUS: a comparative study. Mech. Res. Commun. 78, 71–78.
Parnell, W.J., Grimal, Q., 2009. The influence of mesoscale porosity on cortical bone anisotropy. Investigations via asymptotic homogenization. J. R. Soc. Interface 6 (30), 97–109.
Razi, H., et al., 2020. Damage tolerance of lamellar bone. Bone 130, 115102.
Reisinger, A.G., Pahr, D.H., Zysset, P.K., 2010. Sensitivity analysis and parametric study of elastic properties of an unidirectional mineralized bone fibril-array using mean field methods. Biomech. Model. Mechanobiol. 9 (5), 499–510.
Reznikov, N., Shahar, R., Weiner, S., 2014. Bone hierarchical structure in three dimensions. Acta Biomater. 10 (9), 3815–3826.
Rho, J.-Y., Kuhn-Spearing, L., Zioupos, P., 1998. Mechanical properties and the hierarchical structure of bone. Med. Eng. Phys. 20 (2), 92–102.
Schwiedrzik, J., et al., 2014. In situ micropillar compression reveals superior strength and ductility but an absence of damage in lamellar bone. Nat. Mater. 13 (7), 740–747.
Schwiedrzik, J., et al., 2017. Nanoscale deformation mechanisms and yield properties of hydrated bone extracellular matrix. Acta Biomater. 60, 302–314.
Schwiedrzik, J.J., Zysset, P.K., 2013. An anisotropic elastic-viscoplastic damage model for bone tissue. Biomech. Model. Mechanobiol. 12 (2), 201–213.
Siegmund, T., Allen, M.R., Burr, D.B., 2008. Failure of mineralized collagen fibrils: modeling the role of collagen cross-linking. J. Biomech. 41 (7), 1427–1435.
Thurner, P.J., et al., 2007. High-speed photography of compressed human trabecular bone correlates whitening to microscopic damage. Eng. Fract. Mech. 74 (12), 1928–1941.
Wang, Y., Ural, A., 2018a. Effect of modifications in mineralized collagen fibril and extra-fibrillar matrix material properties on submicroscale mechanical behavior of cortical bone. J. Mech. Behav. Biomed. Mater. 82, 18–26.
Wang, Y., Ural, A., 2018b. Mineralized collagen fibril network spatial arrangement influences cortical bone fracture behavior. J. Biomech. 66, 70–77.
Wang, Y., Ural, A., 2019. A finite element study evaluating the influence of mineralization distribution and content on the tensile mechanical response of mineralized collagen fibril networks. J. Mech. Behav. Biomed. Mater. 100 https://doi.org/10.1016/j.jmbbm.2019.07.019.
Weiner, S., Traub, W., Wagner, H.D., 1999. Lamellar bone: structure–function relations. J. Struct. Biol. 126 (3), 241–255.
Xu, M., An, B., 2020. An analysis of fracture in staggered mineralized collagen fibril arrays. Int. J. Solid Struct. 193, 535–549.
Yoon, Y.J., Cowin, S.C., 2008. The estimated elastic constants for a single bone osteonal lamella. Biomech. Model. Mechanobiol. 7 (1), 1–11.